Naoaki Yamada, MS, MD • Sattoshi Imakita, MD • Toshiharu Sakuma, RT
Makoto Takamiya, MD

Intracranial Calcification on Gradient-Echo Phase Image: Depiction of Diamagnetic Susceptibility[1]

PURPOSE: To differentiate calcification from hemorrhage on the basis of susceptibility at magnetic resonance imaging.

MATERIALS AND METHODS: Gradient-recalled echo (GRE) phase imaging was performed at 1.5 T in 101 calcified areas (15 in the basal ganglia, 86 out of the basal ganglia) and 39 uncalcified locations (13 choroid plexus and pineal glands, 26 old hemorrhages). Experiments with a small lead particle and a numerical simulation were also performed.

RESULTS: The majority of calcifications outside the basal ganglia (n = 63) revealed a phase shift that represents diamagnetic susceptibility and was similar to the phase shift in the lead particle and to the calculated phase shift for a diamagnetic sphere. All hemorrhages and almost all calcified basal ganglia revealed a phase shift that represents paramagnetic susceptibility. All uncalcified choroid plexus and pineal glands revealed no obvious phase shift. Any location without calcification did not reveal the diamagnetic phase shift.

CONCLUSION: GRE phase imaging differentiated paramagnetic from diamagnetic susceptibility, which was specific for calcification.

Index terms: Brain, calcification, 10.81 • Brain, hemorrhage, 10.367, 10.76 • Brain, MR, 10.1214 • Brain, necrosis, 10.78 • Magnetic resonance (MR), tissue characterization

Radiology 1996; 198:171–178

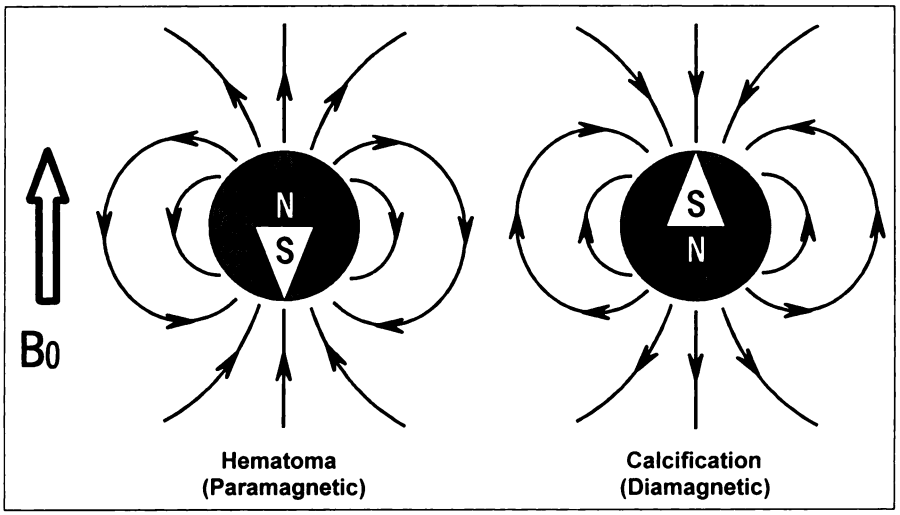

Figure 1. Hematoma and calcification act as magnetic dipoles with opposed orientation to each other.

THE usefulness of magnetic resonance (MR) imaging has been established for intracranial diseases. However, calcifications, which frequently provide important diagnostic information, are more easily and precisely detected with computed tomography (CT). At spin-echo MR imaging, most calcifications are iso- or hypointense to brain tissue and the findings are nonspecific (1–3). Calcium-containing compounds can reduce the proton density, T1, and T2 of free water; hence, calcifications can have high signal intensity on T1-weighted images if the concentration or surface area of calcium-containing compounds is suitable (4,5). However, high signal intensity can appear in laminar necrosis of cerebral infarction as well as in calcification and hemorrhage (6).

Gradient-recalled echo (GRE) imaging is susceptible to static local magnetic field gradients induced by regions that differ in magnetic susceptibility (7,8). Although intracranial calcifications were depicted as markedly hypointense on T2*-weighted images, T2* shortening is not specific to calcification, and a possible additional role of paramagnetic ions in calcified tissues cannot be excluded (8).

GRE phase images can represent the shift of the effective magnetic field at a proton (9–11). Intracerebral hematoma and its environment contain paramagnetic substances such as deoxyhemoglobins, methemoglobins, hemosiderins, and ferritines. On the other hand, bone minerals, dystrophic calcification, and tumoral calcification are mainly composed of calcium hydroxyapatite or apatite-like minerals (12), which may be more diamagnetic than water and brain tissue. Therefore, dipolar field (and phase shift) induced by calcification is expected to be opposed to that induced by hematoma (Fig 1).

We undertook this study to confirm the diamagnetic susceptibility of calcification on GRE phase images and to

[1] From the Department of Radiology, National Cardiovascular Center, 5-7-1, Fujishirodai, Suita, Osaka, 565, Japan. Received March 21, 1995; revision requested May 3; revision received May 31; accepted June 6. **Address reprint requests to** N.Y.

Abbreviations: cgs = centimeter-gram-second, GRE = gradient-recalled echo, TE = echo time, TR = repetition time.

characterize the specific appearance of calcification on MR images.

MATERIALS AND METHODS

Phase shift of a proton ($\delta\phi$) is in proportion to echo time (TE) and perturbation of magnetic field at the proton (δB),

$$\delta\phi = -\gamma \cdot TE \cdot \delta B, \quad (1)$$

where γ is the magnetogyric ratio. We defined $\delta\phi$ as opposite to δB. Therefore, high and low field strengths correspond to negative (dark) and positive (bright) phase shifts, respectively.

Clinical Study

Forty-nine patients were examined with GRE phase imaging. Underlying disease processes in these patients included cerebral infarction (n = 23 patients), intracranial aneurysm (n = 3), intracerebral hemorrhage (n = 3), vascular malformation (n = 3), brain tumor (n = 3), and other (n = 14). Presence or absence of calcification was decided by visually inspecting the CT scans. CT was performed routinely in work-up, with 10-mm (n = 46 patients) or 5-mm (n = 3) section thickness. CT and MR imaging examinations were performed within a 1-month period.

Intracranial locations (n = 140) were studied in the 49 patients. The locations were classified into the following four groups: group 1, calcified locations out of the basal ganglia without evidence of past hemorrhage (n = 86); group 2, uncalcified choroid plexus and pineal glands (n = 13); group 3, calcified locations in the basal ganglia (n = 15); and group 4, old and small hemorrhagic locations without calcification (n = 26) (Table 1).

MR imaging was performed with a head coil on a 1.5-T imager (Magnetom H15; Siemens Medical Systems, Erlangen, Germany). GRE imaging was performed after conventional spin-echo imaging. The GRE

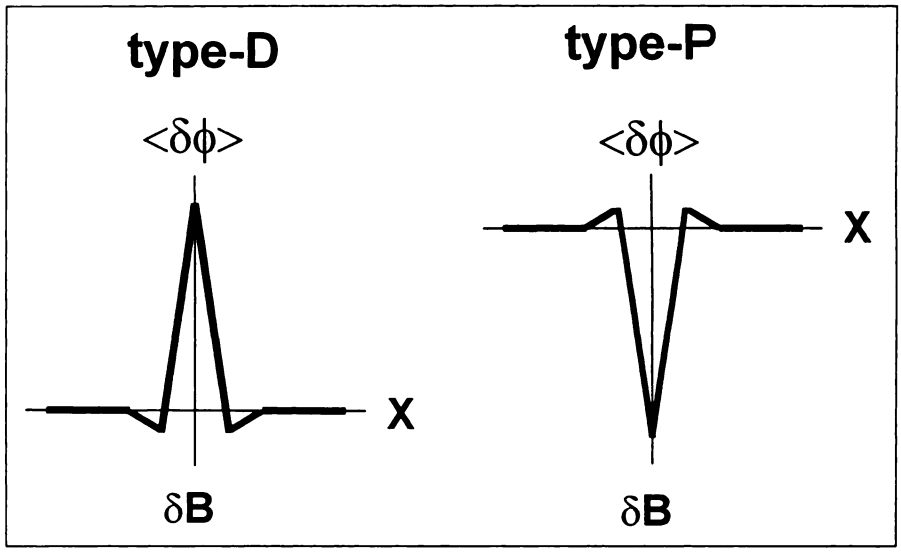

Figure 2. Scheme of types D and P phase shift. In this study, shift of magnetic field (δB_0) is opposed to the phase shift ($\delta\phi$).

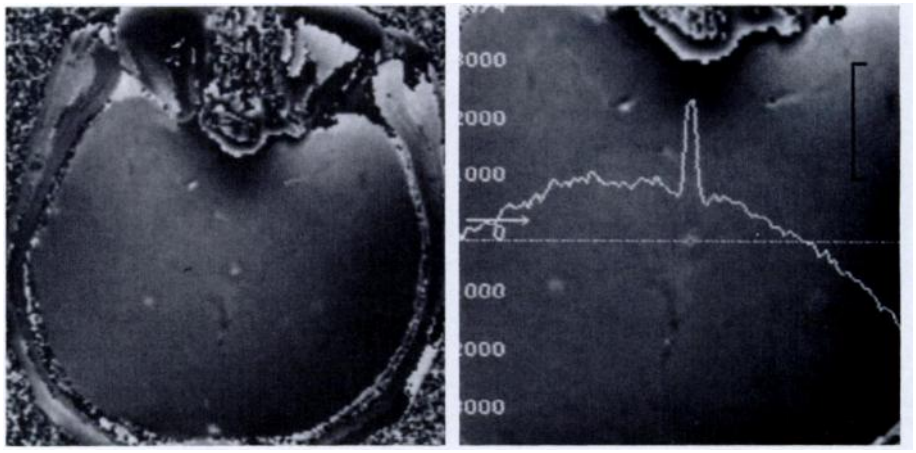

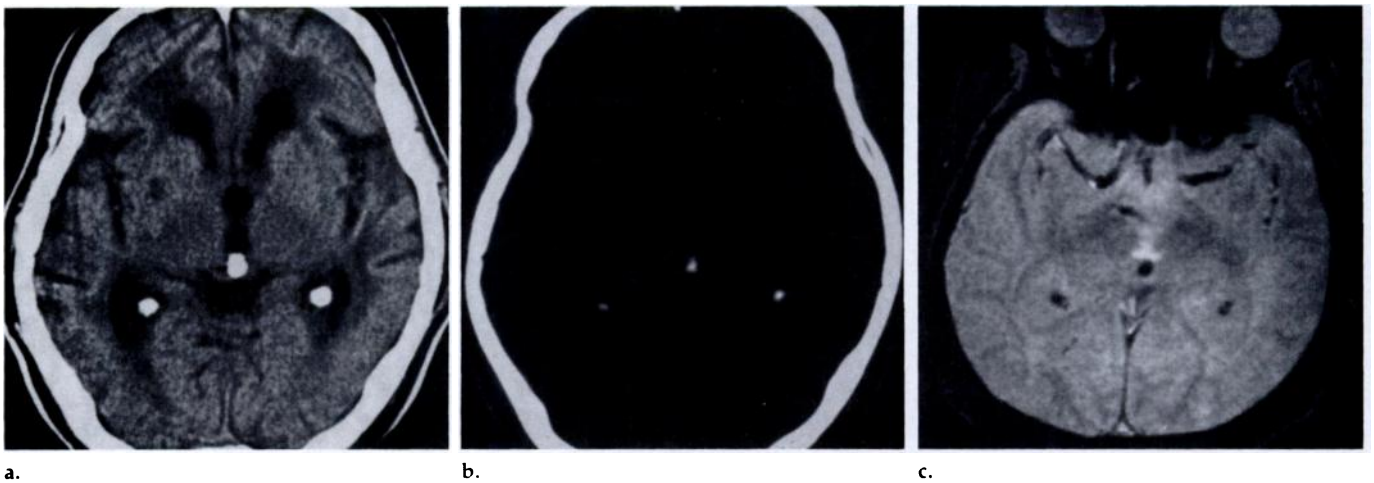

Figure 3. Group 1 location, type D phase shift in a 67-year-old man with multi-infarct dementia. **(a)** Plain CT image obtained with a conventional window (level, 30 HU; width, 80 HU) depicts calcification in the pineal gland and the choroid plexus. **(b)** Plain CT scan obtained with a bone window (level, 300 HU; width, 600 HU) depicts small densely calcified regions. **(c)** GRE image (500/11, with a flip angle of 30°) depicts hypointensity at the calcifications. **(d)** Calcifications on the phase image calculated from the same raw data set as **c** were apparently similar to those in **b**. **(e)** Magnified phase image of **c**, with a profile through a transverse line, revealed type D phase shift. Vertical bar in **e** indicates 90° phase shift (corresponding to 0.35 ppm B_0).

sequence was simple and had a spoiling gradient pulse at the end. Phase and magnitude GRE images were calculated from the same raw data set.

Orientation of the section was perpendicular to the main field and body axis. In all MR imaging examinations, GRE imaging with TE of 11 and/or 30 msec was performed. In 21 MR imaging examinations, GRE imaging with TE of 15 and/or 20 msec was also performed. Repetition time (TR) ranged from 100 to 600 msec. Flip angle ranged from 30° to 70°. In three locations with dense calcification, GRE imaging was performed with fixed TE (11 msec) in all combinations of TR (100, 300, 500 msec) and flip-angle (30°, 50°, 70°). In all examinations, section thickness was 4 mm with an intersection gap of 2 mm, and matrix size was 256 × 256 (the resulting pixel size was 1.0 × 1.0 mm^2).

Phase shift was evaluated with the profile along a 1-pixel-wide line that passed through the center of the location. Maximum phase shift was measured as the difference between the peak and baseline of the profile.

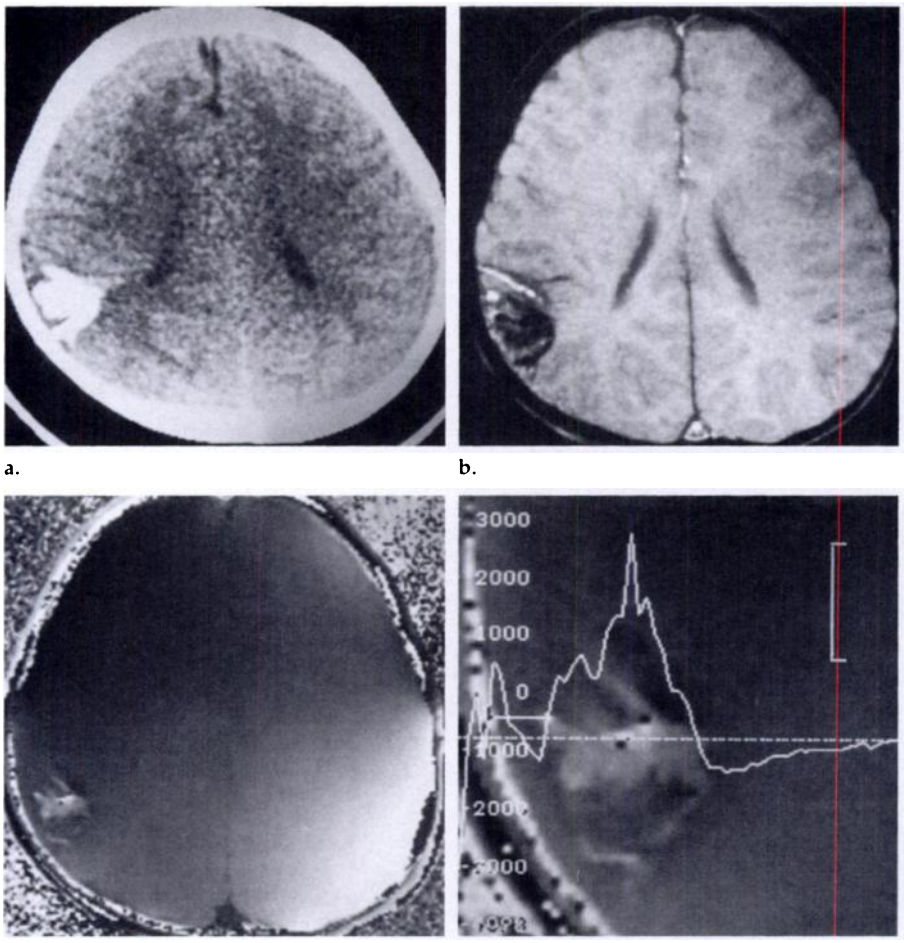

Figure 4. Group 1 location, type D phase shift in a calcified arteriovenous malformation in a 5-year-old boy. **(a)** Plain CT scan depicts a gyriform calcification. **(b)** GRE image (300/20, with a flip angle of 70°) depicts low signal intensity at the calcification. **(c)** Phase image calculated from the same raw data set as **b**. **(d)** Magnified phase image of **c**, with a profile through the calcification, depicts type D phase shift. Vertical bar in **d** indicates 90° phase shift (corresponding to 0.35 ppm B_0).

Table 1
Calcifications in Group 1–4 Locations

	Location of Calcifications						
Group*	Choroid Plexus	Pineal Gland	Tumor	Vascular	Basal Ganglia	Other	Total
1	35	17	7	10	0	17†	86
2	10	3	0	0	0	0	13
3	0	0	0	0	15	0	15
4	0	0	0	0	3	23	26
Total	45	20	7	10	18	40	140

Note.—Numbers are number of calcifications at each location, in each group.
* Group 1, calcified locations out of the basal ganglia; group 2, choroid plexus and pineal glands without calcification; group 3, calcified basal ganglia; group 4, old hemorrhage (hypertensive or idiopathic).
† Locations were the falx (n = 3), tuber of tuberous sclerosis (n = 6), cortex (n = 1 [a patient with Sturge-Weber disease]), and surface of brain (n = 7).

Phantom Experiments

Phantom experiments were performed with the same system as was used in the clinical study. GRE magnitude and phase images were calculated from the same data set. A lead particle (a small sinker used for fishing) that weighed 0.87 g (calculated diameter, on the basis of specific gravity of lead, was 2.5 mm if it was spherical) was hung with nylon string in a spherical flask filled with 5 mmol/L $CuCl_2$ solution in water ($\chi_{CuCl2} \approx 1{,}400 \cdot 10^{-6} \cdot mole^{-1}$ centimeter-gram-second [cgs]). Susceptibility of the solution is almost the same as that of pure water ($\chi_{water} \approx -0.72 \cdot 10^{-6}$ cgs at 20°C). The section was perpendicular to the main field. Section thickness (4 mm) and pixel size (1.0 × 1.0 mm) were fixed. The position of the section in the section-select direction relative to the particle was changed every 2 mm, with fixed TR (100 msec), TE (11 msec), and flip angle (40°). In the section that revealed peak phase shift, the following imaging parameters were changed: TE = 11, 20, 30 msec, with fixed TR (100 msec) and flip angle (40°); TR = 100, 300, 500 msec, with fixed TE (11 msec) and flip angle (40°); flip angle = 30°, 60°, 90°, with fixed TE (11 msec) and TR (100 msec).

Phase shift was evaluated with a 1-pixel-wide profile through the central portion of the particle on the phase images. Signal intensity was evaluated with the profile to determine if it was the same as that of noise on the magnitude images.

Computer Simulation

Consider a diamagnetic sphere placed in water at the center of coordinates. Perturbation of the magnetic field (δB) is the z component of the dipolar field induced by the particle. The coordinates in the read-out (x) and section-select (z) directions are displaced with $\delta B(x,y,z)/G_x$ and $\delta B(x,y,z)/G_z$, respectively, on the image (14). The coordinate in the phase-encode direction (y) is not displaced. Therefore, the coordinate on the image (ξ,η,ζ) is related to the coordinate in real space (x,y,z), with

$$\xi(x, y, z) = x + \delta B(x, y, z)/G_x,$$
$$\eta(x, y, z) = y,$$
$$\zeta(x, y, z) = z + \delta B(x, y, z)/Gz, \quad (2)$$

where G_x and G_z are the read-out and section-select gradients, respectively.

The complex signal of a voxel (M) with its center at (X,Y,Z) may be calculated by summing the complex signal of a small cube with its center at (x,y,z). If the displaced coordinate (ξ,η,ζ) is placed in the voxel, the signal of the cube should be summed; otherwise, it should not be summed. Therefore, we introduce a function

$$F(x, y, z, X, Y, Z) = 1, \text{ if } (\zeta, \gamma, \xi) \text{ is in the voxel,}$$
$$= 0, \text{ if } (\zeta, \gamma, \xi) \text{ is out of the voxel.} \quad (3)$$

Then

$$M(X, Y, Z) = d^3 \cdot \Sigma_x\Sigma_y\Sigma_z F(x, y, z, X, Y, Z) \cdot \rho(x, y, z) \cdot \exp[i \cdot \delta\phi(x, y, z)], \quad (4)$$

where d is the length of the side of the cube,

$$\delta\phi(x, y, z) = -\gamma \cdot TE \cdot \delta B(x, y, z), \quad (5)$$

$$\delta B(x, y, z) = 4\pi \cdot (\cos^2\theta - 1/3) \cdot \delta X \cdot B_0 \cdot a^3/(x^2 + y^2 + z^2)^3, \quad (6)$$

where θ is the angle made by the main field and a vector (x,y,z), a is the radius of the sphere, and ρ is a proton-density function: ρ is 1 if (x,y,z) is out of the sphere and 0 if (x,y,z) is in the sphere. Net phase shift of a voxel ($<\delta\phi>$) may be calculated as phase of M.

Numeric calculation was performed (Mathcad 3.1; MathSoft, Mass) on a personal computer (Contura 25/cx; Compaq, Texas). Consider a spherical particle with 1.25-mm radius and a 4-mm-thick section perpendicular to the main field, with a pixel size of 1.0 × 1.0 mm². Consider gradient pulses with strengths the same as those used in the clinical and phantom studies, $G_x = 3.132 \cdot 10^{-6}$ T/mm and $G_z = 6 \cdot 10^{-6}$ T/mm. We calculated $<\delta\phi>$ for $\delta\chi \equiv \chi_{sphere} - \chi_{water} = 0, -0.05, -0.1, -0.2, -0.3, -0.4, -0.5 \cdot 10^{-6}$ cgs, with fixed TE (11 msec). Z and X were changed every 1 mm and Y was fixed at 0. The amount of increase of x, y, and z in the summation with Equation (4) was 0.1 mm.

RESULTS

Clinical Study

The profile of the phase shift was classified into the following four types (Fig 2): type D (representing diamagnetic susceptibility), advanced phase shift that corresponds to low magnetic field, with or without slight phase retardation in its peripheral portion; type P (a mirror image of type D, representing paramagnetic susceptibility), retarded phase shift that corresponds to high magnetic field, with or without slight phase advancement in its peripheral portion; type H, heterogeneous phase shift; and type O, no obvious phase shift.

Correlation between the types of susceptibility and the groups of locations is summarized in Table 2. Almost all group 1 locations revealed type D (63 of 86 locations) or type O (19 of 86 locations) phase shift (Figs 3, 4). Group 1 locations with type O phase shift had small or thin calcification. All group 2 locations (control group) revealed type O phase shift. All but two group 3 and 4 locations revealed type P phase shift (Figs 5, 6). One group 1 location with type H phase shift had massive and heterogeneous calcifications in a craniopharyngioma. Two group 3 locations with type H phase shift were bilateral globus

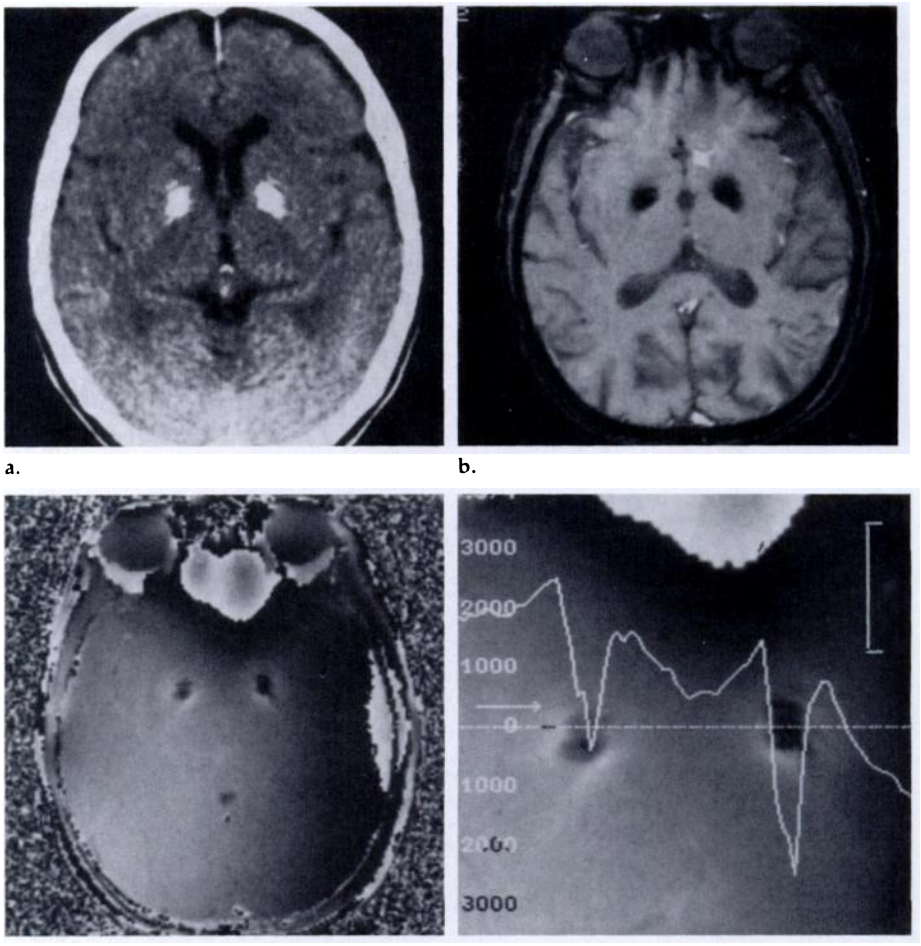

Figure 5. Group 3 location, type P phase shift in a 79-year-old woman with suspected parkinsonism. **(a)** Plain CT scan depicts bilaterally calcified globus pallidus. **(b)** GRE image (200/11, with a flip angle of 70°) depicts hypointensity in the globus pallidus. **(c)** Phase image calculated from the same raw data set as **b**. **(d)** Magnified phase image of **c**, with a profile through the globus pallidus, depicts type P phase shift. Vertical bar in **d** indicates 90° phase shift (corresponding to 0.35 ppm B_0).

Table 2
Type of Phase Shift in Each Location

Group*	Type of Phase Shift				Total
	D	P	H	O	
1	63	3	1	19	86
2	0	0	0	13	13
3	0	13	2	0	15
4	0	26	0	0	26
Total	63	42	3	32	140

Note.—Numbers are number of areas with each type of phase shift, per group. D = diamagnetic, P = paramagnetic, H = heterogeneous, O = no obvious phase shifts.
* Group 1, calcified locations out of the basal ganglia; group 2, choroid plexus and pineal glands without calcification; group 3, calcified basal ganglia; group 4, old hemorrhage (hypertensive or idiopathic).

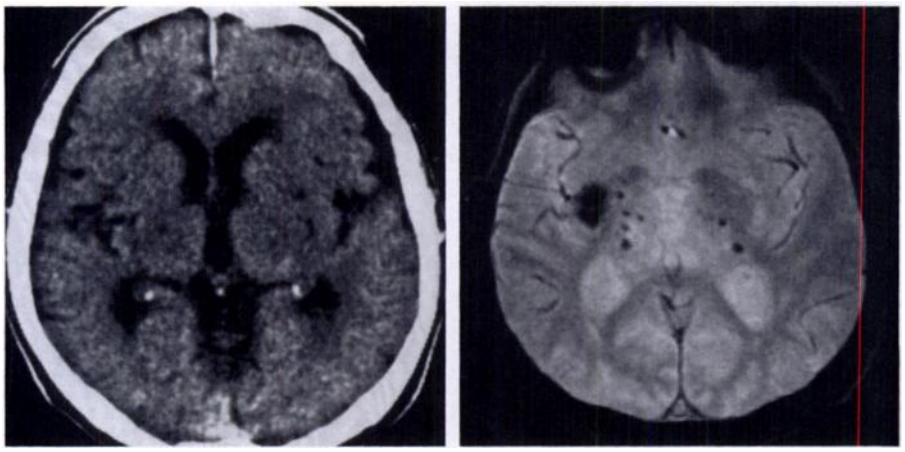

a. b.

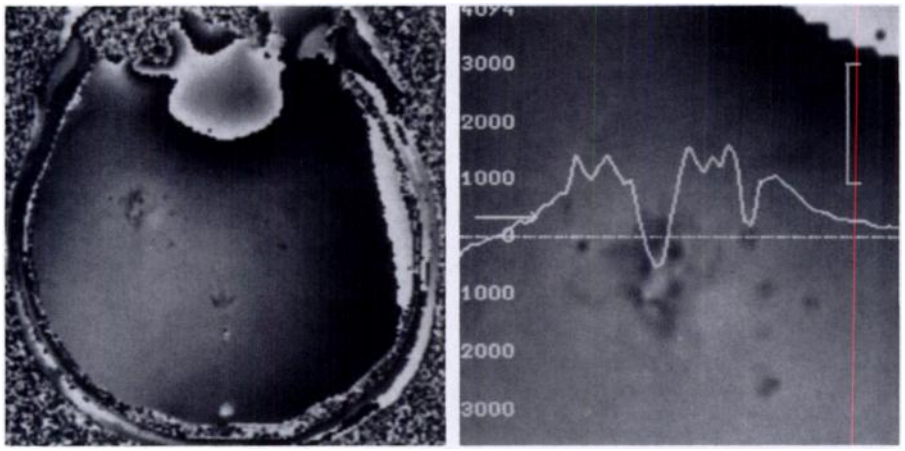

c. d.

Figure 6. Group 4 location, type P phase shift, and group 1 location, type O phase shift were both seen in a 79-year-old man with a long history of hypertension who had experienced right putaminal hemorrhage, which was depicted at CT performed 6 years before these images were obtained. **(a)** Plain CT scan depicts fine calcifications in the choroid plexus and pineal gland and no calcification in the basal ganglia and thalamus. **(b)** GRE image (600/11, with a flip angle of 30°) depicts multiple hypointense lesions (small old hemorrhages) in the basal ganglia and thalamus. **(c)** Phase image calculated from the same raw data set as **b** depicts phase retardation that corresponds to the hypointense lesions. The calcifications did not reveal obvious phase shift even in the neighboring sections (type O phase shift). **(d)** Magnified phase image of **c**, with a profile through a transverse line, depicts type P phase shift at the hypointense lesions. Vertical bar in **d** indicates 90° phase shift (corresponding to 0.35 ppm B_0).

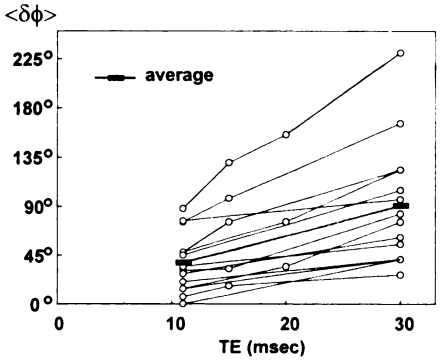

Figure 7. Maximum (type D) phase shift in type D locations in group 1 increased almost linearly with TE. Horizontal bars indicate the average at TEs of 11 and 30 msec.

pallidus with calcification in an 18-year-old woman with familial ataxia. Three group 1 locations with type P phase shift were calcified choroid plexus.

In 13 locations with type D phase shift, the maximum phase shift was measured with two to four TEs, including both 11 and 30 msec (Fig 7). The maximum phase shift was almost proportional to TE and was independent of TR and flip angle. In the locations with small phase shift, imaging with longer TE was effective to confirm the shift. We decided that a location had type O phase shift if it had no obvious phase shift even with TE of 30 msec.

Phantom Experiment

The lead particle revealed type D phase shift. Phase shift increased with TE (Fig 8). However, phase shift at TE of 20 msec was only 1.5 times as much as phase shift at 11 msec (phase shift was not linearly related to TE). Phase shift at TE of 30 msec had a notch at the central portion where the signal intensity was nearly as low as the level of noise. Phase shift was independent of TR and flip angle and depended on the position of the imaging section relative to the lead particle. Peripheral phase retardation was obvious when the particle was placed near the center of the section but was not obvious when the particle was placed off center. More detailed phantom experiments with lead particles have been reported (13).

Computer Simulation

Phase shift $<\delta\phi>$ was type D at each $\delta\chi$ (Fig 9a). Peak amplitude of $<\delta\phi>$ initially increased with $\delta\chi$ and saturated at large $\delta\chi$ (Fig 9b). Amplitude of $<\delta\phi>$ substantially changed if X and Z were shifted slightly (Fig 9c, 9d).

Unfortunately we could not find any value for the susceptibility of calcified particle or hydroxyapatite in the literature. With the Pascal formula, Wehrli et al (7) estimated susceptibility of calcium hydroxyapatite (χ_{apa}) and water (χ_{water}) as $-0.876 \cdot 10^{-6}$ and $-0.583 \cdot 10^{-6}$ cgs, respectively, which resulted in the difference, $\delta\chi = \chi_{apa} - \chi_{water} = -0.293 \cdot 10^{-6}$ cgs. With a measured susceptibility for water ($-0.72 \cdot 10^{-6}$ cgs), the difference is $-0.156 \cdot 10^{-6}$ cgs. Since susceptibility of lead (χ_{Pb}) is $-1.247 \cdot 10^{-6}$ cgs, the difference, $\delta\chi = \chi_{Pb} - \chi_{water}$, is $-0.527 \cdot 10^{-6}$ cgs. The measured phase shift of the lead particle was smaller than the calculated phase shift (Figs 8, 9), probably because of the slightly off-center position in the section, the unspherical shape of the particle, and contamination with metals other than lead.

DISCUSSION

Clinical Usefulness of Phase Imaging

Results in our clinical study showed that all locations of type D phase shift at GRE imaging had calcification (100% specificity of type D for calcification). The fact that the phase shift is almost independent of TR and flip angle can be an advantage of phase imaging, because the interpretation is simple. It takes no excess imaging time to obtain phase images.

Sufficiently T2*-weighted images (TR second/TE msec = 0.2–0.75/50, with a flip-angle of 10°) depicted all calcifications as having low signal intensity (8). In this study, many small or thin group 1 calcifications had type O phase shift (phase shift was not obvious). Small phase shift should have

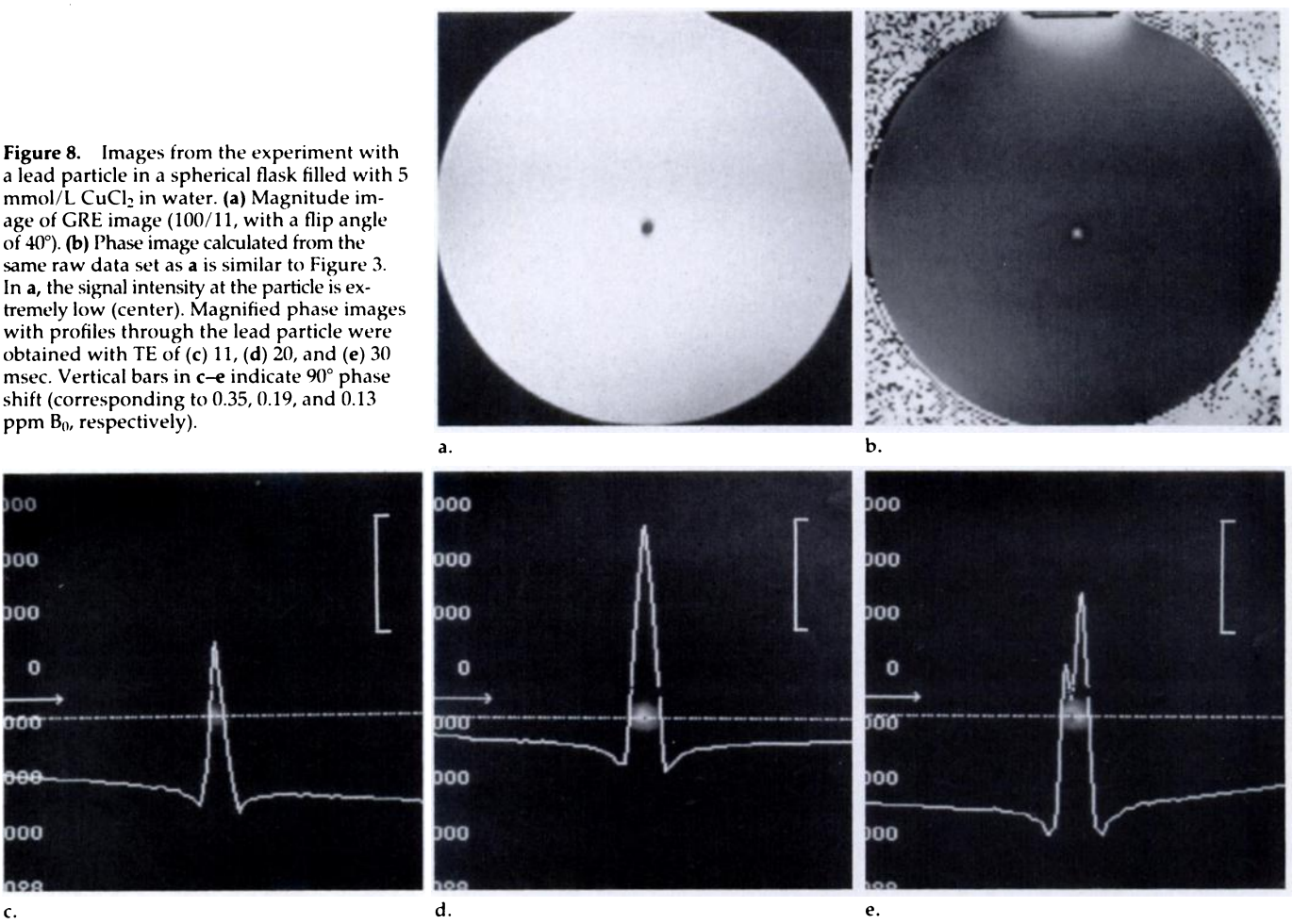

Figure 8. Images from the experiment with a lead particle in a spherical flask filled with 5 mmol/L $CuCl_2$ in water. **(a)** Magnitude image of GRE image (100/11, with a flip angle of 40°). **(b)** Phase image calculated from the same raw data set as **a** is similar to Figure 3. In **a**, the signal intensity at the particle is extremely low (center). Magnified phase images with profiles through the lead particle were obtained with TE of (**c**) 11, (**d**) 20, and (**e**) 30 msec. Vertical bars in **c–e** indicate 90° phase shift (corresponding to 0.35, 0.19, and 0.13 ppm B_0, respectively).

been masked by the perturbation of phase shift due to noise and artifacts. More heavily T2*-weighted (TE ≥ 50 msec), or less noisy (eg, low-bandwidth data sampling) phase images might have revealed type D phase shift in the fine calcifications. In small calcifications, use of small voxels would be effective to enhance the phase shift. We confirmed that phase shift increases as voxel size decreases, in experiments with lead particles (13). All old and small hemorrhages, which are frequently found in patients with hypertension, revealed type P phase shift. A sequential study of symptomatic intracerebral hematoma on GRE phase images demonstrated that chronic hematoma usually has a ring-shaped phase shift around it (11). However, we found that many small hematomas finally reveal type P phase shift (Fig 6).

Calcifications contain various trace metals such as copper, iron, manganese, zinc, calcium, and phosphorous (15–20). However, to our knowledge, the magnetic properties of these metals are not known. If a calcification is accompanied by abundant paramagnetic substances, it may reveal type P phase shift. In this study, however, group 1 calcifications had mostly type D phase shift (ie, diamagnetic components were dominant). The cause of type P phase shift of the three group 1 choroid plexus is not known, but there is a possibility of asymptomatic hemorrhage. Iron accumulates in the basal ganglia, especially in the globus pallidus, and the concentration increases with age (21–24). Type P phase shift of calcified group 3 globus pallidus can be ascribed to depositions of paramagnetic irons. In these locations, findings with CT and MR imaging compensate each other: CT is sensitive to calcification and MR imaging is sensitive to paramagnetic substances. The presence of type H calcified globus pallidus in a young female patient may be due to insufficient accumulation of iron, which results in competition between diamagnetic and paramagnetic components.

A few limitations of phase imaging should be mentioned. If the signal intensity of a calcification is extremely low, measurement of the phase shift is not reliable, because it should be affected by noise and artifacts. If the shape of a calcification is extremely irregular, the phase shift will be heterogeneous. If a calcification is suspected to be on the surface of the brain, flow signal of cortical artery and vein should be ruled out. Phase shift due to flow can be positive (type D) or negative (type P), depending on flow velocity and geometry. To differentiate calcification and flow, magnitude images are helpful. Although there was a tendency for denser calcifications to have larger phase shifts than did finer calcifications, quantitative evaluation of the phase shift is not as effective in clinical practice because the geometric factors are too complex.

Mechanisms of Phase Shift

The microscopic structure of calcifications is complex: large stones are seen in Fahr disease (16), clustered psammoma bodies are seen in choroid plexus and meningioma (17), and a mixture of amorphous and grape-like structures is seen in the pineal gland (18). Local magnetic field should be inhomogeneous, depending on the shape, size, and distribution of calcified particulates as well as on susceptibility differences (7,10,14,25).

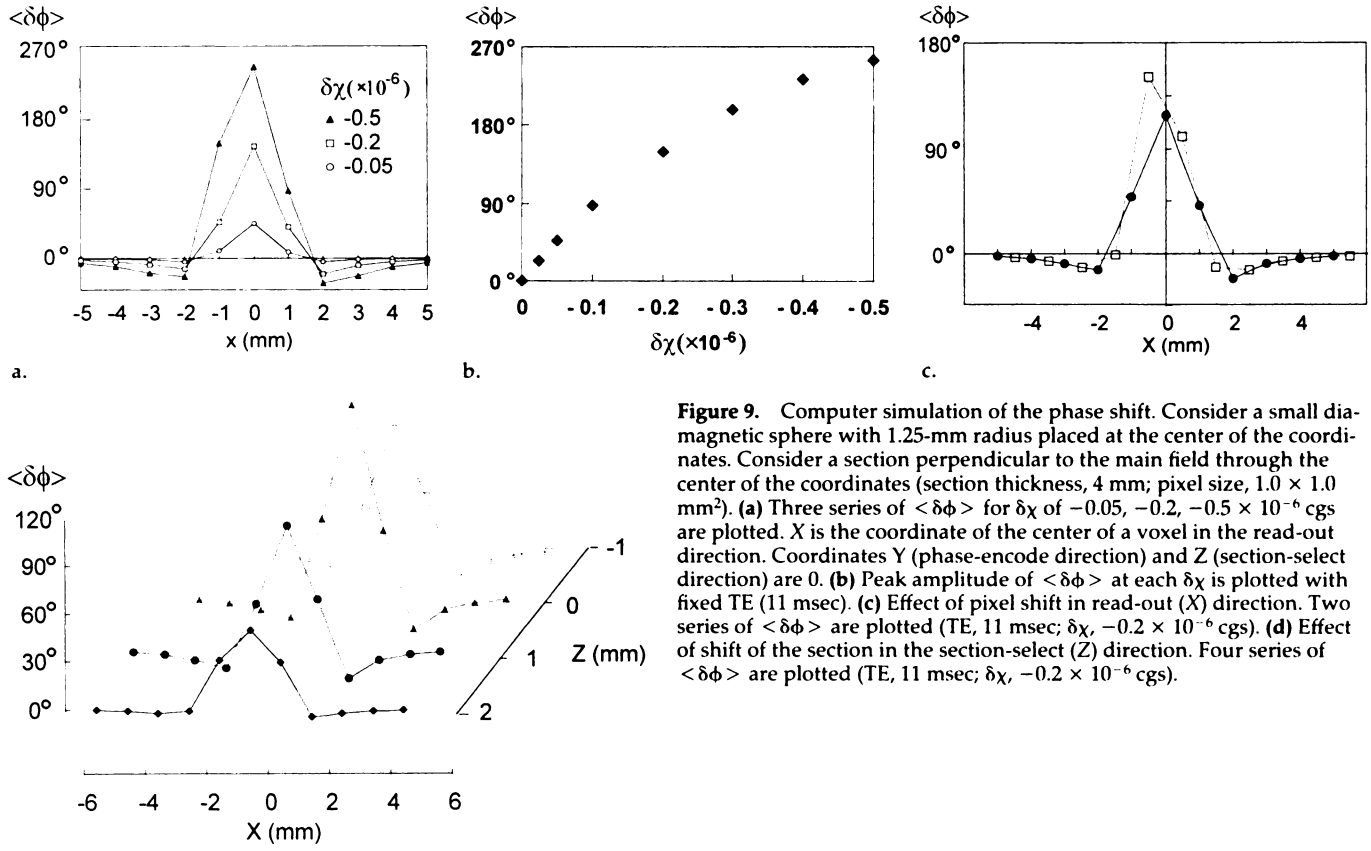

Figure 9. Computer simulation of the phase shift. Consider a small diamagnetic sphere with 1.25-mm radius placed at the center of the coordinates. Consider a section perpendicular to the main field through the center of the coordinates (section thickness, 4 mm; pixel size, 1.0 × 1.0 mm^2). **(a)** Three series of $<\delta\phi>$ for $\delta\chi$ of -0.05, -0.2, -0.5×10^{-6} cgs are plotted. *X* is the coordinate of the center of a voxel in the read-out direction. Coordinates Y (phase-encode direction) and Z (section-select direction) are 0. **(b)** Peak amplitude of $<\delta\phi>$ at each $\delta\chi$ is plotted with fixed TE (11 msec). **(c)** Effect of pixel shift in read-out (*X*) direction. Two series of $<\delta\phi>$ are plotted (TE, 11 msec; $\delta\chi$, -0.2×10^{-6} cgs). **(d)** Effect of shift of the section in the section-select (*Z*) direction. Four series of $<\delta\phi>$ are plotted (TE, 11 msec; $\delta\chi$, -0.2×10^{-6} cgs).

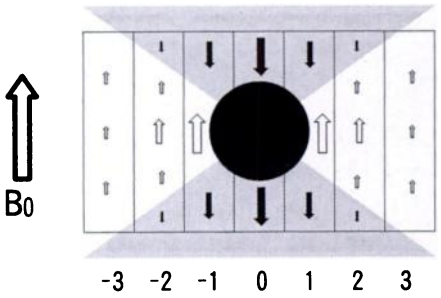

Figure 10. A scheme of the mechanisms of phase shift. Consider a diamagnetic particle (●) placed at the center of the coordinates. Perturbation of the magnetic field δB (the z component of the dipolar field induced by the particle) is antiparallel to the main field in the superior and inferior side (solid arrows) and is parallel to the main field in the lateral side (open arrows). Voxels are illustrated with rectangles (−3 to 3). In the central voxel (*0*), δB is negative (positive phase shift). In the voxel including the lateral border of the particle (*−1, 1*), positive and negative δB cancel out each other, which results in small positive or negative net phase shift. In the more lateral voxels (*−2, −3, 2, 3*), small positive δB is dominant (small negative phase shift).

Roughly speaking, however, densely calcified portions should have low signal because free water content is very low and T2* is very short. The area of no or less calcification that surrounds the area of dense calcification should respond to the dipolar field induced by the dense portion and should dominate the signal intensity in the voxel including the calcification. Phase shifts in high and low field strengths must cancel each other out in a voxel that includes lateral border of the dense portion (Fig 10).

The phase shift of a proton ($\delta\phi$) is in proportion to both TE and $\delta\chi$ (Eqq [5, 6]). However, if $\delta\phi$ exceeds $\pm 180°$, it is projected in the range within $\pm 180°$. Therefore, the average phase shift in a voxel ($<\delta\phi>$) can be nonlinear to $\delta\chi$ and TE if $\delta\phi$ diverges over $\pm 180°$ (Fig 9b). This fact is critically different from the fact that the average phase shift of the magnetic field in a voxel (δB) is linear to $\delta\chi$.

We do not know of any study that found the chemical shift of free water proton in biologic tissue to be substantially different from the chemical shift of pure water. The small or no difference in phase shift between brain tissue and cerebrospinal fluid (Figs 3–6) supports the hypothesis that chemical shift of water proton in brain tissue is almost the same as that in pure water. Chemically inactive stones (calcifications) seem not to effect the chemical shift of bulk water. Findings in our experiments with precipitation of hydroxyapatite and calcium carbonate particulates in water (not published) suggest that chemical shift due to the particulates was negligible compared with the effect of susceptibility. We believe the phase shifts we observed in calcification were predominantly caused by susceptibility effect.

In conclusion, T2*-weighted GRE images cannot differentiate diamagnetic location (eg, calcification) from paramagnetic location (eg, hemorrhage) because both have low signal intensity, but GRE phase images can differentiate them. Typically, calcifications reveal positive phase shift (corresponding to negative shift of the magnetic field), which can be specific for calcification, whereas small hemorrhagic lesions reveal negative phase shift (corresponding to positive shift of the magnetic field). Results in numerical calculation and experiments confirmed that diamagnetic particles have a positive phase shift. Averaging the spin of a proton in a voxel is essential to understand the phase shift behavior. ■

References

1. Holland BA, Kucharczk W, Brant-Zawadzki M, Norman D, Haas DK, Harper PS. MR imaging of calcified intracranial locations. Radiology 1985; 157:353–356.
2. Oot RF, New PFJ, Pile-Spellman J, Rosen BR, Shoukimas GM, Davis KR. The detec-

tion of intracranial calcification by MR. AJNR 1986; 7:801–809.
3. Tsuchiya K, Makita K, Furui S, Nitta K. MRI appearances of calcified regions within intracranial tumors. Neuroradiology 1993; 35:341–344.
4. Henkelman RM, Watts JF, Kucharczk W. High signal intensity in MR images of calcified brain tissue. Radiology 1991; 179:199–206.
5. Dell LA, Brown MS, Orrison WW, Eckel CG, Matwiyoff NA. Physiologic intracranial calcification with hyperintensity on MR imaging: case report and experimental model. AJNR 1988; 9:1145–1148.
6. Boyko OB, Burger PC, Schelburne JD, Ingram P. Non-heme mechanisms for T1 shortening: pathologic, CT and MR elucidation. AJNR 1992; 13:1439–1445.
7. Wehrli FW, Ford JC, Attie M, Kressel HY, Kaplan FS. Trabecular structure: preliminary application of MR interferometry. Radiology 1991; 179:615–621.
8. Atlas SW, Grossman RI, Hackney DB, et al. Calcified intracranial lesions: detection with gradient-echo-acquisition rapid MR imaging. AJNR 1988; 9:253–259.
9. Young IR, Bydder GM, Khenia S, Collins A. Assessment of phase and amplitude effects due to susceptibility variations in MR imaging of the brain. J Comput Assist Tomogr 1989; 13:490–494.
10. Yamada N, Imakita S, Sakuma T, et al. Evaluation of the susceptibility effect on the phase images of a simple gradient echo. Radiology 1990; 175:561–565.
11. Yamada N, Imakita S, Nishimura T, Takamiya M, Naito H. Evaluation of the susceptibility effect on gradient echo phase images in vivo: a sequential study of intracerebral hematoma. Magn Reson Imaging 1992; 10:559–571.
12. Anderson HC. Calcification processes. Pathol Annu 1980; 15:45–75.
13. Lüdeke KM, Röschmann P, Tischler R. Susceptibility artefacts in NMR imaging. Magn Reson Imaging 1985; 3:329–343.
14. Sakuma T, Yamada N, Yamada Y, Doi T. Evaluation of diamagnetic susceptibility effect on magnetic resonance phase images using gradient echo. Jpn J Radiol Technol 1995; 51:118–124. [Japanese]
15. Löwenthal A, Bruyn GW. Calcification of the striopallidodentate system. In: Vinken PJ, Bruyn GW, eds. Handbook of clinical neurology. Amsterdam, The Netherlands: North Holland, 1986; 417–436.
16. Smeyers-Verbeke J, Michotte Y, Pelsmaeckers J, et al. The chemical composition of idiopathic nonarteriosclerotic cerebral calcifications. Neurology 1975; 25:48–57.
17. Alcolado JC, Moore IE, Weller RO. Calcification in the human choroid plexus, meningiomas and pineal gland. Neuropathol Neurol 1986; 12:235–250.
18. Michotte Y, Löwenthal A, Knaepen L, Collard M, Massart DL. A morphological and chemical study of calcification of pineal gland. J Neurol 1977; 215:209–219.
19. Kojik M, Kulczycki J. Laser-spectrographic analysis of the cation content in Fahr's syndrome. Arch Psychiatr Nervenkr 1978; 225:135–142.
20. Duckett S, Galle P, Escourolle R, Poirier J, Hauw JJ. Presence of zinc, aluminium, magnesium in striopalledodentate (SPD) calcifications (Fahr's disease): electron probe study. Acta Neuropathol (Berl) 1977; 38:7–10.
21. Hallgren B, Sourander P. The effect of age on the non-haemin iron in the human brain. J Neurochem 1958; 3:41–51.
22. Drayer BP, Burger P, Darwin R, et al. Magnetic resonance imaging of brain iron. AJNR 1986; 7:373–380.
23. Chen JC, Hardy PA, Clauberg M, et al. T2 values of human brain: comparison with quantitative assays of iron and ferritin. Radiology 1989; 173:521–526.
24. Aoki S, Okada Y, Nishimura K, et al. Normal deposition of brain iron in childhood and adolescence: MR imaging at 1.5 T. Radiology 1989; 172:381–385.
25. Yablonskiy DA, Haarke EM. Theory of NMR signal behavior in magnetically inhomogeneous tissues: the static dephasing regime. Magn Reson Med 1994; 32:749–763.